Intrinsic viscoelasticity of C-S-H assessed from basic creep of cement pastes

Zhangli Hu[a,b,*], Adrien Hilaire[a,c], Julien Ston[a], Mateusz Wyrzykowski[b], Pietro Lura[b,d], Karen Scrivener[a]

[a] Laboratory of Construction Materials, EPFL, Lausanne CH-1015, Switzerland
[b] Empa, Swiss Federal Laboratories for Materials Science and Technology, Dübendorf CH-8600, Switzerland
[c] GEOTEST AG, Zollikofen CH-3052, Switzerland
[d] Institute for Building Materials, ETH Zurich, Zurich CH-8092, Switzerland

ARTICLE INFO

ABSTRACT

This paper investigates the fundamental mechanisms behind the effect of supplementary cementitious materials (SCMs) on the basic creep behavior of cement pastes. The intrinsic creep properties of the C-S-H gel are assessed based on measurements of uniaxial compressive basic creep of cement pastes with different water-to-cement ratio (w/c), prepared either with pure cement or cement blended with fly ash or quartz. The viscoelastic response of the C-S-H was back-calculated from the macroscopic experimental creep results with Finite Element Method (FEM) homogenization. The numerical simulations show that the intrinsic viscoelastic behavior of the C-S-H gel follows a similar trend in different systems, independent of their w/c (in the range 0.35–0.63) and the binder used. The differences in the magnitude of the creep at the macroscopic scale in different cement-based systems appear to depend mainly on the volumetric fractions of the solid phases and on the porosity of the cement pastes.

1. Introduction

Delayed strains in concrete (including different types of shrinkage and creep) are one of the main issues related to the aging of concrete structures. One of the components of the delayed strain is creep. In order to separate the effect of creep and shrinkage strains, creep is often measured on systems subject to a constant stress and protected from desiccation or from moisture ingress at constant temperature, so-called *basic creep*. Basic creep of concrete has been extensively investigated and a large amount of data is available in the literature (e.g., [1–4]). However, the creep of concrete is mainly governed by the creep of the cement paste, while the aggregates are supposed to show only elastic response [5,6]. For this reason, this work is performed at the cement paste level (e.g., [3,4]).

Many modern concrete structures incorporate blended cements, which include supplementary cementitious materials (SCMs). The effect of SCMs on the basic creep of concrete has however received only limited attention. Among the few studies that exist on the basic creep compliance, fly ash, slag and silica fume are the mostly investigated SCMs. The main observation is that concretes with different mineral additives show different creep behavior compared to Portland cement concrete, especially in the case of loading at very early ages [7–9]. In

systems with silica fume, for example, the early age creep increased proportionally to the degree of cement replacement by silica fume [8]. The addition of fly ash also enhanced the creep of concrete; this effect is more pronounced with higher fly ash substitution levels [7,9]. On the contrary, in the work of Pane and Hansen [8], the basic creep compliance was reduced by the presence of fly ash and slag but not by silica fume. Different trends were also found in the case of replacing cement with slag. Ji et al. [7] showed that slag had no significant effect on the development of the creep compliance in compression, while the results by Shariq et al. [10] show a certain effect. Altogether, the impact of SCMs on the basic creep compliance is unclear in the published literature and almost no work has been done on the underlying mechanisms. All effects found in the literature are roughly interpreted as originating from the microstructure, the strength or the interfacial properties of the SCMs - albeit without clear and specific evidence about the acting mechanisms.

As calcium-silicate-hydrate (C-S-H) is commonly considered to be the main creeping phase in cementitious systems containing C-S-H [11,12], clarifying the mechanisms of the viscoelastic behavior at the C-S-H level is essential.

The aim of this study is to investigate the intrinsic viscoelastic behavior of C-S-H, in particular shed light on the effect of both SCMs (fly

Table 1
Oxides composition and physical properties of materials used.

Oxides compositions (mass %)	PC	QZ	FA
SiO_2	20.45	99.83	69.67
Al_2O_3	4.39	–	23.8
Fe_2O_3	3.01	0.03	2.39
CaO	64.48	0.02	0.1
MgO	1.66	–	0.2
SO_3	2.83	–	0.01
Na_2O	0.24	–	0.09
K_2O	0.89	0.05	0.61
TiO_2	0.34	0.02	1.51
P_2O_5	0.28	–	0.14
Mn_2O_3	0.05	–	0.05
ZrO_2	–	0.01	–
LOI.	1.3	0.02	0.95
Physical properties			
Density (g/cm^3)	3.12	2.63	2.17
D_{50} (μm)	13	12	16
Specific surface area (m^2/g)	1.15	1.17	1.20

Table 3
Compressive strength and static Young's modulus.

	Compressive strength (MPa)	Static Young's modulus (GPa)
PC35	90.0 ± 2.0	18.5 ± 0.5
PC40	72.0 ± 3.2	16.1 ± 0.1
CQZ35	54.0 ± 1.0	17.1 ± 0.4
CFA35	70.0 ± 1.8	18.3 ± 0.6

ash or quartz filler) and water-to-cement ratio (w/c, in the range 0.35–0.63) on creep. The creep of C-S-H is obtained by back calculation from the cement paste scale (at this scale the simulation is fitted to the experimental creep data) based on the assumption that the paste is composed of intrinsically viscoelastic C-S-H gel, porosity and elastic inclusions (other hydration products, unhydrated cement, SCM/fillers). Hence, the simulations were performed at two microstructural scales: 1) cement paste scale with the Finite Element Method (FEM) framework AMIE [13] using 2D geometries with circular inclusions representing different phases embedded in a continuous C-S-H matrix and 2) at the C-S-H matrix scale (composed of C-S-H gel and capillary porosity) using estimations of the effect of porosity on mechanical properties from [14], where microstructural modelling focused on the effect of different morphologies of porosity/solids.

2. Materials and mixture proportions

In this study, the materials used were ordinary Portland cement, quartz filler and fly ash. The chemical and physical properties of all materials are listed in Table 1. The Portland cement (CEMI 42.5R, labeled as PC) was produced in Switzerland. Quartz filler (QZ) employed to replace clinker has a particle size distribution comparable to PC (the median particle sizes, D_{50}, of all materials are listed in Table 1). Class-F fly ash (FA) had a fairly low reactivity (after 28 days, its degree of reaction is about 20% at 20 °C [15]).

The creep behavior of four different mixtures was investigated. Their mix proportions are presented in Table 2. Three mixtures were cast with w/b equal to 0.35 and one with w/b of 0.40. The w/c in these four mixtures is in the range of 0.35–0.63. The two Portland cement pastes with different w/c were labeled as PC35 and PC40, respectively. For w/b = 0.35, the replacement level of fly ash was 40% by mass (specimen CFA35), while the amount of quartz filler (specimen CQZ35) was adjusted to keep the same level of volumetric replacement (49% by volume).

Table 2
Mixture proportions for cement pastes specimens.

Mass (g)	PC	water	QZ	FA
PC35	100	35	–	–
PC40	100	40	–	–
CQZ35	55.25	35	44.75	–
CFA35	60	35	–	40

3. Basic creep properties of cement pastes

3.1. Experimental methods

3.1.1. Compressive strength and static Young's modulus

The strength of cement pastes determined from compressive tests was used to quantify the load level to be applied during basic creep measurements in compression. Prismatic specimens with size of $40 \times 40 \times 160 \, mm^3$ were cast and cured at $20 \pm 0.1 \, °C$ and $\geq 95\%$ RH. They were cut into $40 \times 40 \times 40 \, mm^3$ cubic samples with a diamond saw using water as lubricant after one day of curing. All samples were sealed after being cut and they were tested at 28 days. At least three specimens were used for each mixture. The mean results and the standard deviation are presented in Table 3.

The static Young's modulus was estimated as the loading modulus in compression based on standard [16] on prismatic specimens of $40 \times 40 \times 160 \, mm^3$. The results are shown in Table 3. The specimens were sealed with paraffin films and the wrapping was removed only just before the tests.

3.1.2. Autogenous shrinkage

In order to obtain the basic creep, the linear autogenous shrinkage strains were measured and subtracted from the total creep results. Corrugated tubes with 29 mm diameter and length of 425 mm based on ASTM C1698-09 were used [17]. The corrugated tubes filled with pastes were sealed with polyethylene plugs of 19 mm length. The tubes were vibrated shortly during the filling process to ensure that the air bubbles were removed. During the measurements, the tubes were submerged in a silicone oil bath to avoid possible drying through the tubes/plugs and to enable efficient temperature control at $20 \pm 0.1 \, °C$. The longitudinal deformation was measured at one free end by one LVDT. The low stiffness of the molds minimizes the restraint on the cement paste, while enclosing the pastes in the molds almost eliminates moisture loss [18]. The presented results are the average of duplicate samples.

The mass loss at the end of the tests was below 0.03% for each tube, which ensures the good quality of the sealing of the specimens during the experiments [17,19]. In all, the measurement of the long-term autogenous shrinkage was only minimally influenced by the additional drying shrinkage due to imperfect sealing.

3.1.3. Compressive creep tests

Uniaxial compressive creep tests were performed on cement pastes with metal creep frames with lever mechanism, as shown in the schematic sketch in Fig. 1.

Specimens of $25 \times 25 \times 80 \, mm^3$ were cast and demolded after about 20 h. They were sealed immediately with polyethylene film and self-adhesive aluminum foil. The samples were weighed before and after the experiments to control the mass loss. Two loading plates helped to fix the position of the specimen and of the LVDTs. Two steel balls with diameter of 13 mm connected the loading plates and the lever, which was designed to distribute and balance the applied load [20]. Three LVDTs were positioned around a sample and attached to the loading plates to monitor the deformation. The load was added manually at the other end of the lever. The advantage of this loading method is that it is possible to obtain uniform, quasi-instantaneous and
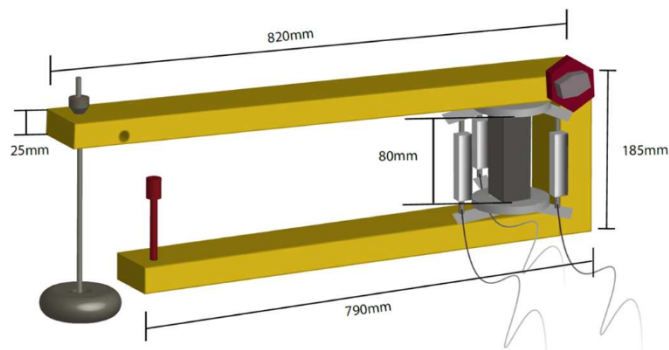
Fig. 1. Schematic view of the creep frame.

Fig. 2. Autogenous shrinkage evolution after 28d.

accurate load. Duplicate specimens were tested for each system. The creep tests were performed in a temperature-controlled room ($T = 20 \pm 0.3\,°C$). The data was logged at 1 s intervals in the first 15 min after each loading step and 2 min afterwards.

The specific basic creep strain was calculated according to the following equation:

$$\varepsilon_{bc}(t) = \varepsilon_{meas}(t) - \varepsilon_{ins}(t) - \varepsilon_{au}(t) \qquad (1)$$

The specific creep recovery, $\varepsilon_{bc}{}^{rec}$, if the sample is unloaded at $t = \tau_{un}$, is defined according to Eq. (2).

$$\varepsilon_{bc}^{rec}(t) = \varepsilon_{meas}(\tau_{un}) - \varepsilon_{meas}(t) + \varepsilon_{au}(t) - \varepsilon_{au}(\tau_{un}) - \varepsilon_{ins}(\tau_{un}) \qquad (2)$$

where ε_{meas} is the total strain measured from the basic creep test, ε_{ins} is the strain occurring in the loading phase and ε_{au} is the autogenous strain measured with the corrugated tubes. The specimens were loaded at $\tau = 28$ days and unloaded at 56 days. After unloading, the creep recovery strain was recorded. The stress-to-strength ratio used was 0.1. This low ratio ensures that creep is linearly dependent on the applied stress σ_0 [5].

Eq. (1) was established by assuming that the strain measured in the loading phase (so-called instantaneous strain) was identical with the elastic strain of the material. The loading modulus determined in this way was very close (< 1 GPa difference) to the static Young's modulus estimated based on the standard [16] (see Section 3.1.1). This is to be expected, considering that both methods used similar loading rates, with loading phases lasting seconds to minutes. It should be stressed here that the modulus determined in this way necessarily underestimates the actual Young's modulus, as the strains measured in the loading phase are not only elastic but include the visco-elastic-visco-plastic strain, see [21,22].

The basic creep compliance $J(\tau, t)$ and the specific basic creep compliance $C(\tau, t)$ functions are defined by Eqs. (3) and (4):

$$J(\tau, t) = \frac{\varepsilon_{meas}(t) - \varepsilon_{au}(t)}{\sigma_0} \qquad (3)$$

$$C(\tau, t) = \frac{\varepsilon_{meas}(t) - \varepsilon_{au}(t) - \varepsilon_{ins}(t)}{\sigma_0} \qquad (4)$$

The specific basic creep recovery function, $C_{rec}(\tau_{un}, t)$ is defined by Eq. (5).

$$C_{rec}(\tau_{un}, t) = \frac{\varepsilon_{bc}^{rec}(t - \tau_{un})}{\sigma_0} \qquad (5)$$

The mass loss at the end of the tests was lower than 0.08% for all samples. Based on the data published by Hansen for a Portland cement paste with w/c 0.4, this mass loss would induce an additional drying shrinkage of about 30 μm/m [23]. The expected impact of unwanted drying is estimated to have been only around 1% of the total measured strain. The delayed strain associated to drying (drying shrinkage and drying creep) was thereafter neglected.
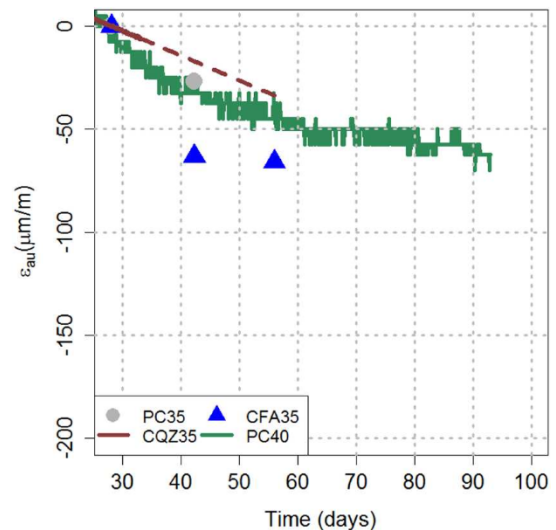
3.2. Experimental results and discussions

3.2.1. Autogenous shrinkage

The long-term autogenous shrinkage, ε_{au}, of the different systems is presented in Fig. 2. This paper focuses on the long-term delayed strains in sealed conditions. Therefore, the results shown here were zeroed at the age of loading of the samples (28 days). For PC35 and CFA35, the autogenous shrinkage was measured manually (shown as symbols in Fig. 2). For PC40, the autogenous shrinkage was measured continuously with LVDTs. For the system CQZ35, the autogenous shrinkage was only recorded continuously during the first 6 days of the basic creep test. Therefore, an extrapolation was calculated assuming that the trend of the curve does not change to estimate the evolution of the autogenous strain during the duration of the test (dashed line). Since the overall autogenous shrinkage CQZ35 was small, this extrapolation would not cause significant influence on the calculations of the basic creep of the system.

One month after the casting of the specimens, the rate of autogenous shrinkage was very small compared to the first days of hydration. However, compared to the total delayed strain, the autogenous shrinkage was not small enough to be neglected in the calculation of the basic creep compliance.

3.2.2. Compressive basic creep compliance

The measured uniaxial creep compliances and the specific basic creep compliance are plotted as a function of time in Figs. 3 and 4 for all systems. Note that the autogenous shrinkage was around 10% of the total creep deformation in all systems. For the Portland cement pastes without any SCM, the higher the w/c, the higher the creep was. The dependence of the basic creep behavior on the w/c is well known in the literature, where it is considered to be due to either higher water content or higher porosity in systems with higher w/c [3,24].

For w/b = 0.35, the creep behavior was apparently strongly linked to the type of mineral admixture used to replace cement. Compared to the ordinary Portland cement system, the cement pastes containing either fly ash or quartz filler had higher creep compliance. A similar effect of filler and fly ash has already been noticed for concrete [25].

3.2.3. Kinetics analysis of basic creep

3.2.3.1. Tikhonov regularization.
Based on a direct examination of the creep compliance data, it is difficult to extract common trends between all of these cementitious systems, especially quantitative trends. Several studies suggested that it is more relevant to analyze the derivative of the creep compliance, which can provide quantitative comparisons
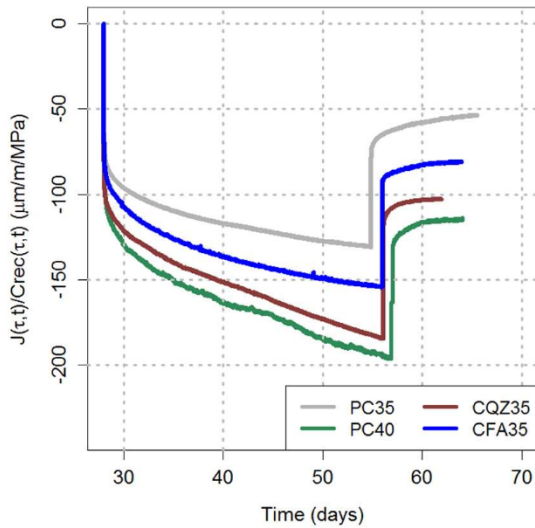
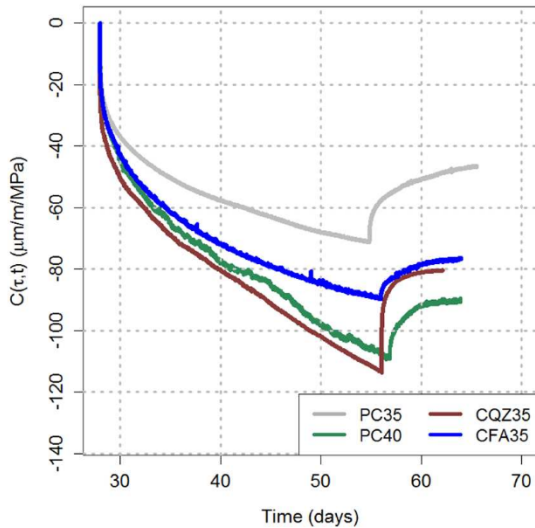Fig. 3. Basic creep compliance and creep recovery.

Fig. 4. Specific basic creep compliance and creep recovery.

[4,26]. Instead of using direct differentiation of the experimental curves to obtain the first derivative of the creep compliance, the kinetics of creep compliance was calculated with a Tikhonov regularization [27]. The principle of the method is to convert the problem into solving an integral equation within a large amount of uniformly-spaced data points that are generated from the experimental results. By minimizing the linear error combination equation considering both the deviation of the computed value from the raw data and the square of the second derivative at the interior discretization points, the first derivative of the equation can be found. The regularization parameter in the linear error combination equation was selected by using a 10-fold cross-validation technique [28]. Note that this method does not require any assumption about the functional form of the data and leads to smooth results compared to direct derivation.

3.2.3.2. Results and power law expression. The first derivative of the specific creep compliance with respect to time using Tikhonov regularization method, $dC(\tau,t)/d(t-\tau)$, is plotted on a log-log scale in Fig. 5. It should be noted that time in the plot refers to the duration of the creep not to the age of the samples. The advantage of this choice of differentiation is that it enables identification of a single relationship to describe the basic creep behavior [4,29].
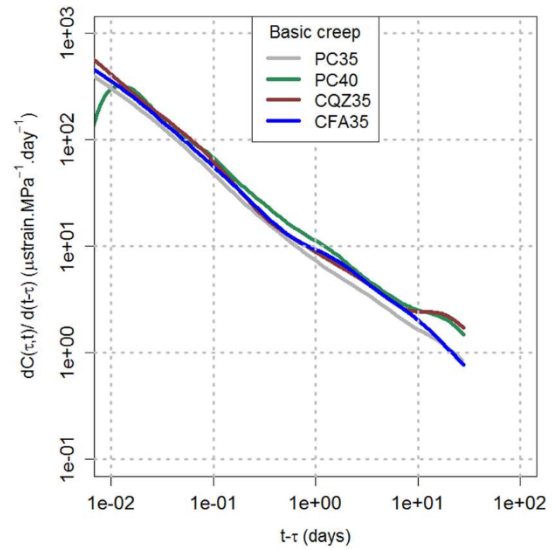

Fig. 5. Derivative of the specific basic creep compliance.

This representation of the results highlights that the kinetics of creep compliance in the time period considered (4 weeks under load) can be modelled by a power-law equation [4]:

$$\frac{dC_{\mathrm{mod}}(\tau,t)}{d(t-\tau)} = A\left(\frac{t_1}{t-\tau}\right)^{\gamma} \quad \text{for } t-\tau > 10^{-2}\text{day} \tag{6}$$

where γ is a power-law exponent, and A is a constant. t is sample age and τ is the loading time, t_1 is the time unit. C_{mod} is the modelled specific basic creep compliance, which is therefore calculated as follows:

$$C_{\mathrm{mod}}(\tau,t) = \frac{A}{1-\gamma} \times (t-\tau)^{1-\gamma} + B \quad \text{for } t-\tau > 10^{-2}\text{day} \tag{7}$$

The constant B is determined according to the following equation:

$$C_{\mathrm{mod}}(t-\tau = 10^{-2}) = C_{\mathrm{exp}}(t-\tau = 10^{-2}) \tag{8}$$

in which the function C_{exp} is the measured specific basic creep compliance.

The amplitude of the very short-term creep kinetics is very sensitive to the definition of the instantaneous creep compliance [30]. Additionally, the value of the creep rate was not sensitive to this parameter for stress durations longer than about 15 min. Therefore, the creep kinetics was only plotted for $t - \tau > 10^{-2}$ d (~15 min). The determined values by fitting the experimental creep curve with Eq. (6) are presented in Table 4. The creep exponent γ seemed to vary little between cementitious systems, remaining between 0.68 and 0.78. The w/c and the presence of SCMs did not appear to affect this parameter significantly. On the contrary, the parameter A, which corresponds to the creep compliance rate at 1 day, was strongly affected by the composition of the cement paste.

4. Downscaling the basic creep properties of cement pastes

Using the experimental creep results detailed in Section 3 as input,

Table 4
Parameters A, γ and B.

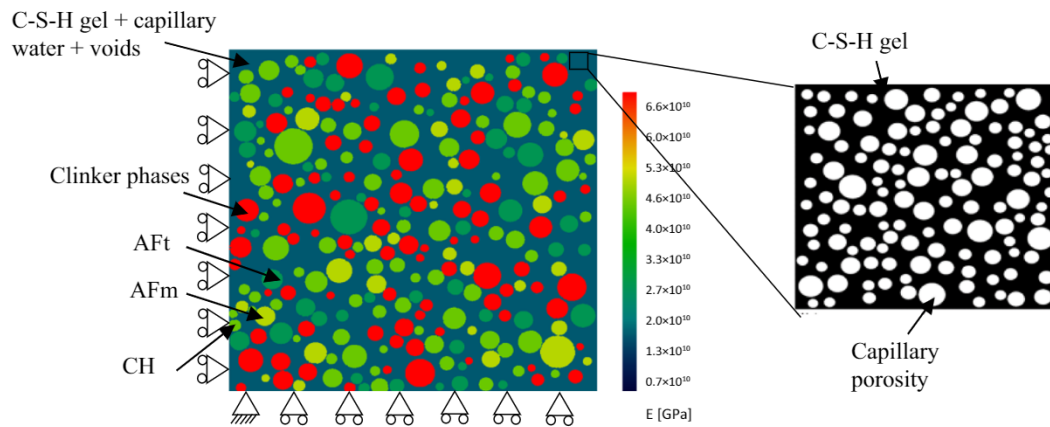|	A ($10^{-6}\cdot\text{MPa}^{-1}\cdot\text{d}^{-1}$)	γ (–)	B ($10^{-6}\cdot\text{MPa}^{-1}$)
PC35	−8.567	0.755	3.5
PC40	−12.125	0.6863	1.5
CQZ35	−11.499	0.723	−3.5
CFA35	−10.123	0.754	4.0

Fig. 6. Two-scale simulation computational cell (PC35), with color indicating the stiffness of each phase (in [Pa]). The boundary conditions used in the simulations are also presented.

the viscoelastic properties of C-S-H upon loading are back-calculated for four mixtures (PC35, PC40, CQZ35 and CFA35) using microstructural simulations (2D) and microstructural modelling results from [14].

4.1. Microstructural simulation method

Cement paste can be regarded as a two-scale composite material (see Fig. 6), for which it is assumed that the viscoelastic behavior is originating solely at the C-S-H level:

- At the cement paste scale, the main elastic phases including clinker phases,[1] CH (portlandite), AFt (ettringite), AFm (monosulfate) and fly ash or quartz (when used) are represented as circular inclusions and do not experience any viscoelastic behavior. A hypothesized particle size distribution of the elastic phases (normal distribution with mean of 5.5 μm and standard deviation of 1.85 μm) was used. In fact, the effect of different particle size distributions or different shapes of the inclusions on the results was negligible [31], as long as reasonable particle size distributions were employed (e.g., the largest particle is smaller than 0.25 of the size of the computational cell [32]). In the present study, the inclusions are considered to be circular in order to simplify the 2-D simulation [31]. The elastic phases are embedded into a viscoelastic matrix made of C-S-H gel (C-S-H with interlayer and gel water), capillary water and voids. The viscoelastic behavior of this matrix is back-calculated thanks to 2D numerical simulations performed with the FEM framework AMIE [13]. The size of the computational cell is $100 \times 100\,\mu m^2$.
- At a smaller scale, the C-S-H matrix scale, the mixture is composed of C-S-H gel and capillary porosity. This mixture is described as a porous material. The gel phase is made of C-S-H with its interlayer water and gel porosity (gel water). The microstructure of this mixture is discussed later.

The volume fractions of the different phases including C-S-H (with interlayer water) and capillary and gel porosity were determined by mass balance. The whole procedure follows the method described in [33] with some modifications for determining the composition of the C-S-H:

- Reacted oxides (CaO, SiO_2, Al_2O_3, Fe_2O_3, MgO, SO_3 and CO_2) were estimated by subtracting the remaining oxides after hydrating for 28 days from the initial oxides in the systems. The initial oxides

were obtained from the X-ray fluorescence analysis of the raw materials and the mix design. Remaining oxides were derived from the X-ray diffraction with Rietveld quantification of cement pastes at 28 day.
- MgO was used to determine the amount of hydrotalcite $(Mg_4Al_2O_7(H_2O)_{10})$, subtracting the amount of Al_2O_3 and H_2O in hydrotalcite from the total reacted oxides.
- Fe_2O_3 was used to determine the amount of hydrogarnet $((CaO)_3$ (Fe_2O_3) (SiO_2) $_{0.84}$ (H_2O) $_{4.32})$, subtracting the amount of CaO, SiO_2 and H_2O in hydrogarnet from the remaining reacted oxides.
- The remaining reacted SiO_2 was used to calculate the amount of C-S-H. The chemical composition of the C-S-H was estimated based on the Ca/Si and Al/Ca obtained from Scanning Electron Microscopy and Energy Dispersive X-ray Spectroscopy (SEM-EDS) measurements. The volumetric ratio of interlayer water and gel water was measured with [1]H Nuclear Magnetic Resonance (NMR) and both types of water were considered as intrinsic parts of the C-S-H. The interlayer water amount in the C-S-H was fixed to be 1.8 H_2O [34] in all systems. With this volumetric ratio of two types of water, the amount of gel water can be also calculated. The amounts of CaO, Al_2O_3 and H_2O in the C-S-H were subtracted from the remaining reacted oxides.
- The amount of AFt was measured by X-ray diffraction with Rietveld quantification. The amounts of CaO, Al_2O_3, SO_3 and H_2O in AFt were subtracted from the remaining reacted oxides. The remaining SO_3 was bound in AFm and the remaining CaO was bound in CH.
- After subtracting the water bound in the determined phases, the amount of capillary water was calculated. Chemical shrinkage measurements were also carried out to estimate the amount of the empty voids (results were zeroed at the time of final set).

The calculated volume fraction and density of the phases considered in the microstructural simulation are listed in Table 5. The comparison of the volume of capillary pores (total porosity) calculated from mass balance is shown in Table 6 and compared to the total porosity measured with Mercury Intrusion Porosimetry (MIP) to provide a rough validation of the calculations. The MIP measurements were performed with the maximum pressure of 400 MPa and a contact angle of 120° was assumed. For all four systems, the porosities obtained from the two methods were in very good agreement.

4.2. Cement-paste scale

The elastic Young's modulus and Poisson's ratio of different phases used in the simulation are listed in Table 7. Note that the elastic Young's modulus of fly ash was calculated using the modulus of the glass phases in the fly ash reported in [35]. With the quantities determined from

---

[1] Clinker phases include C_3S (tricalcium silicate), C_2S (dicalcium silicate), C_3A (tricalcium aluminate) and C_4AF (tetracalcium aluminoferrite).

Table 5
The density and input volume fraction of phases in systems for the simulation.

Cement-paste scale	C-S-H matrix	Clinker phases	CH	AFm	AFt	QZ	FA
Density (g/cm³)	–	3.13	2.11	1.98	1.80	2.63	2.17
PC35	0.60	0.14	0.13	0.05	0.08	–	–
PC40	0.60	0.11	0.15	0.06	0.09	–	–
CQZ35	0.50	0.02	0.15	0.04	0.04	0.24	
CFA35	0.59	0.05	0.04	0.03	0.05	–	0.23
C-S-H matrix scale	C-S-H gel	Capillary porosity					
Density (g/cm³)	2.00	1.00					
PC35	0.71	0.29					
PC40	0.64	0.36					
CQZ35	0.54	0.46					
CFA35	0.68	0.32					

Table 6
Comparison of the cement paste porosity measured by MIP and capillary porosity calculated from mass balance.

	Mass balance	MIP
PC35	0.17	0.18
PC40	0.21	0.25
CQZ35	0.23	0.23
CFA35	0.19	0.19

Table 7
Elastic Young's modulus and Poisson's ratio of phases considered in the simulation.

	Elastic Young's modulus (GPa)	Poisson's ratio (−)	References
Clinker phases	130.0	0.300	[39]
CH	38.0	0.305	[40]
AFt	22.4	0.255	[40]
AFm	42.3	0.324	[40]
water and voids	0.001	0.500	[40]
QZ	70.0	0.150	[41]
FA	72.0	0.210	[35]

SEM-EDS following the method presented in [36], a self-consistent scheme was applied to compute the stiffness of the fly ash. The Poisson's ratio of C-S-H was assumed to be 0.24 [37]. The rheology model, a Kelvin-Voigt chain of 5 units with characteristic times (τ_n) of 0.002, 0.02, 0.2, 2, 20 and 200 days, was used to mathematically describe the viscoelastic response of the C-S-H matrix. These specific characteristic times were set to capture both the short-term and the long-term creep. The discretization was both formulated in space and in time by using connected time slabs/blocks in the FEM meshes with their structure reflecting the assembled springs and dashpots (see detailed algorithm in

[38]). The values of stiffness of the springs in the Kelvin-Voigt chain are calibrated based on the macroscopic creep results, see Table 8. The relationship between the viscosity of the dashpot ($\eta_n(t)$) and the stiffness of the spring ($E_n(t)$) is $\eta_n(t) = E_n(t) \times \tau_n$.

4.3. C-S-H matrix and C-S-H gel scales – elastic properties

The first step of the microstructural simulation is to estimate the elastic modulus of the C-S-H matrix from the experimental results of the cement paste. This was done with the microstructures generated based on volume fractions of different phases (Fig. 6) and the mechanical properties from Table 7 by trial and error with the *AMIE* framework.

The calculated elastic moduli of the C-S-H matrices for the four systems studied are listed in Table 9. According to the simulation, the elastic Young's modulus of the C-S-H matrix was in the range of 8 to 13 GPa. Additionally, the solid fractions within the C-S-H matrix calculated based on porosity (see Section 4.1) are also presented. It can be readily seen that the elastic Young's modulus of the C-S-H matrix is higher for higher solid fractions.

Thus, the next step concerned estimating the elastic Young's modulus of the underlying C-S-H gel from the upper-scale of the C-S-H matrix. This step could not be carried out using explicit microstructural modelling, because modelling of the C-S-H gel with its porosity would require explicitly describing the gel pores and the complex morphology of the C-S-H sheets/needles, which is beyond the capabilities of the present FEM model and in fact beyond the present knowledge of the C-S-H morphology. Instead, microstructural modelling results from [14] were applied. Roberts and Garboczi [14], based on finite element modelling of generated 3D microstructures, established the ratios between the elastic deformations of a solid matrix and a porous body (these ratios are further referred to as the *scale factors*). In particular, the microstructures were generated in [14] using different statistical models, providing different morphologies of porosity/solids. Seven statistical models for generating different 3D microstructures including four Gaussian random field models (GRF) and three Boolean models were considered in [14]. The four GRF models are called single-cut, two-cut, open cell intersection and closed-cell union models respectively, with different solid phase region in the simulated space. The three Boolean models are overlapping solid spheres, spherical pores and oblate spheroidal pores, respectively, considering different shapes of solids and pores [14]. The ratios between the elastic strains of the porous bodies and the solids expressed as a function of solid fraction resulting from these models are presented in Fig. 7.

When the values of the scale factor estimated with the two-cut GRF model [14] are used, the estimated elastic moduli of the C-S-H gel lie in the range 22–28 GPa (for other GRF models similar, but lower values are found), see Table 9. These values seem reasonable considering the experimental evidence [11,37], where about 21 GPa was found for low density C-S-H and about 31 GPa for high density C-S-H. It should be noted that in our simulations a single type of C-S-H is used.

Other factors, in particular the chemical composition of the C-S-H, could also affect its elastic and viscoelastic properties. Due to the

Table 8
Stiffnesses of springs and viscosities of dashpots used in Kelvin-Voigt chains for different systems.

Specimens	$E_{0.002}(t)$ (Pa)	$E_{0.02}(t)$ (Pa)	$E_{0.2}(t)$ (Pa)	$E_2(t)$ (Pa)	$E_{20}(t)$ (Pa)	$E_{200}(t)$ (Pa)
PC35	2.0×10^{11}	1.2×10^{11}	9.7×10^{10}	7.4×10^{10}	2.6×10^{10}	2.2×10^{10}
PC40	2.4×10^{11}	1.2×10^{11}	8.0×10^{10}	6.4×10^{10}	1.4×10^{10}	1.1×10^{10}
CFA35	0.8×10^{11}	1.4×10^{11}	1.5×10^{11}	5.5×10^{10}	1.9×10^{10}	2.8×10^{10}
CQZ35	1.0×10^{11}	1.0×10^{11}	6.8×10^{10}	9.0×10^{10}	1.9×10^{10}	4.8×10^9
Specimens	$\eta_{0.002}(t)$ (Pa·day)	$\eta_{0.02}(t)$ (Pa·day)	$\eta_{0.2}(t)$ (Pa·day)	$\eta_2(t)$ (Pa·day)	$\eta_{20}(t)$ (Pa·day)	$\eta_{200}(t)$ (Pa·day)
PC35	4.0×10^8	2.4×10^9	1.9×10^{10}	1.5×10^{11}	5.2×10^{11}	4.4×10^{12}
PC40	4.8×10^8	2.4×10^9	1.6×10^{10}	1.3×10^{11}	2.8×10^{11}	2.2×10^{12}
CFA35	1.6×10^8	2.8×10^9	3.0×10^{10}	1.1×10^{11}	3.8×10^{11}	5.6×10^{12}
CQZ35	2.0×10^8	2.0×10^9	1.4×10^{10}	1.8×10^{11}	3.8×10^{11}	9.6×10^{11}

Table 9
Elastic Young's moduli of C-S-H matrix and C-S-H gel, solid fraction and selected scale factors.

	C-S-H matrix (GPa)	Solid fraction (in C-S-H matrix)	Scale factor (two-cut GRF)	C-S-H gel (GPa)
PC35	12.62	0.71	0.52	24.3
PC40	10.75	0.64	0.42	25.6
CQZ35	8.61	0.54	0.31	27.8
CFA35	10.40	0.68	0.47	22.1
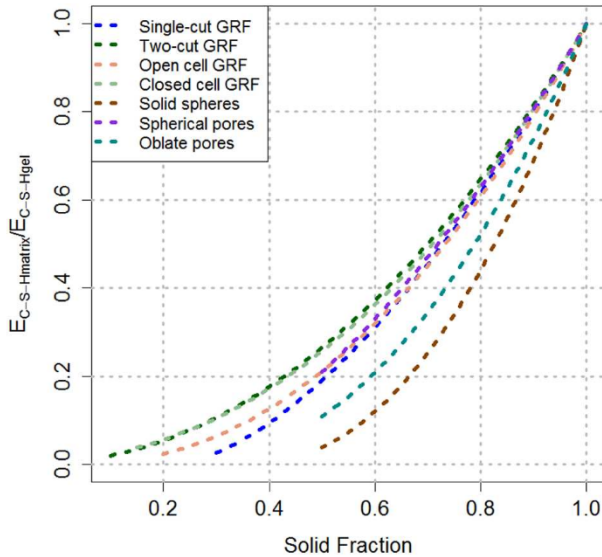
Fig. 7. Ratio between elastic Young's modulus of C-S-H matrix and C-S-H gel (scale factor) as a function of solid fraction.

Fig. 8. Back-calculated specific basic creep compliance of C-S-H matrix and C-S-H gel in PC35.

presence of fly ash, the Ca/Si is lower and the Al/Ca is higher [42]. For lower Ca/Si, the stiffness of C-S-H might be expected to decrease based on nano-indentation measurements [43]. A lower bulk modulus was also observed when the Ca/Si was lower in [44], while others observed that the effect of Ca/Si is minor [45]. The dependence of the elastic Young's modulus upon Ca/Si could explain the lower value of the elastic Young's modulus of the fly ash system CFA35.

Another factor that could influence the elastic Young's modulus of the C-S-H gel is the amount of gel porosity, which may differ depending on the degree of hydration reached [46] and likely also depending on the composition of the paste. Based on the mass balance calculations, the gel porosities in the C-S-H gel were equal to: 0.118, 0.129, 0.126 and 0.137 for PC34, PC40, CFA35 and CQZ35, respectively. For such small differences (the maximum difference from the average did not exceed 8%), this effect should be of minor importance in the pastes tested here.

4.4. C-S-H matrix – viscoelastic properties

It was assumed that the scale factor of the elastic deformations (ratio between the elastic deformations of the solid matrix and the porous body) is also valid for the viscoelastic deformations:

$$\varepsilon_{elas}^{solids}(\phi)/\varepsilon_{elas}^{porousmedium} = \varepsilon_{viscoelas}^{solids}(\phi)/\varepsilon_{viscoelas}^{porousmedium} \qquad (9)$$

where ϕ is the solid fraction (calculated as 1-porosity).

The assumption expressed with Eq. (9) is naturally an approximation. Different approaches have been applied so far for estimating the effect of porosity on creep (equivalent to the scale factor) of porous materials with intrinsically viscoelastic skeleton. One of the simplest approaches is based on scaling the creep by the stress-increment factor
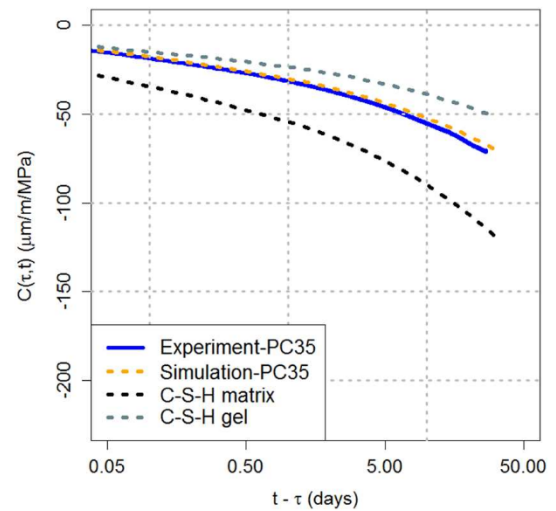
[47]. According to one such approach derived for polycrystalline ceramics [47] for the exemplary case of PC35, with 0.29 porosity (see Table 9), the creep rate of a porous body should be about 60% higher than that of the skeleton. The factor of $1/1.6 = 0.63$ is higher than the scale factor of 0.52 found with the two-cut GRF model. More advanced up-scaling approaches can be based on micromechanics modelling or different homogenization schemes using the correspondence principle [48–50]. A relatively good agreement between the scale factors of elastic (scale factor equal to about 0.38 for porosity of 0.3 and 0.26 for porosity of 0.4) and viscoelastic properties (scale factors equal to about 0.44 and 0.29, respectively) was found with Finite Element simulations in [49]. Therefore, the assumption (Eq. (9)) appears to be justified, in particular considering the uncertainty of the effect of morphology on the scale factor and the fact that we assessed the effect of differences in the scale factor later on, by comparing two extreme cases.

With the scale factor, the viscoelastic response of the C-S-H gel was scaled down from the viscoelastic behavior of the C-S-H matrix. The latter was back-calculated by trial and error from macroscopic creep experiments (see Sections 4.2 and 4.3) at the cement paste scale, using the assumption that the C-S-H matrix is the only component experiencing creep in a cement paste. An example of fitting creep at different scales is presented for PC35 in Fig. 8. In this simulation, the scale factor was taken from the two-cut GRF model. As presented in the figure, after solving the finite element problem, the modelled basic creep compliance agreed well with the experimental results. Also for the other three systems, the modelled creep compliances of the cement pastes were all in good agreement with the experimental results (not presented here).

The corresponding results of specific creep compliance of the C-S-H matrix and the C-S-H gel from four systems are shown in Fig. 9 using the scale factor listed in Table 9 (obtained from the two-cut GRF model). It is clear that the viscoelastic behavior of the C-S-H matrix in different systems was different. On the other hand, the intrinsic creep behavior of the C-S-H gel appeared to be similar in systems with different w/c and with or without fly ash and quartz filler.

5. Discussions

5.1. General considerations on the model

The 1) 2D FEM simulations under plane stress state with 2) spherical elastic inclusions embedded in a continuous C-S-H matrix employed in the present work are substantial simplifications of the actual 3D microstructure of a cement paste, with its complex morphology of
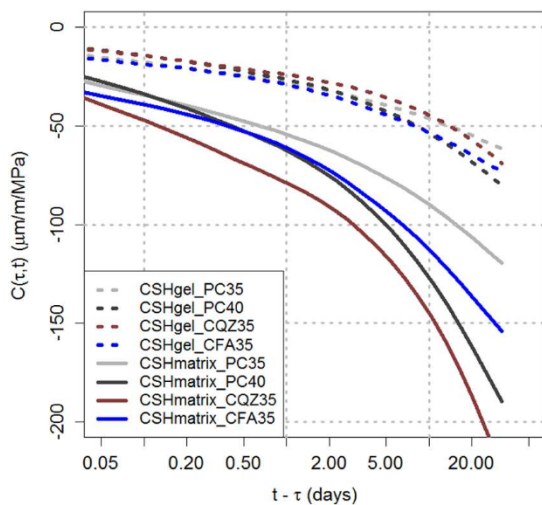
Fig. 9. Comparison of back-calculated viscoelastic behavior (specific basic creep compliance) of C-S-H matrix and C-S-H gel in four systems (scale factor based on the two-cut GRF model, see Fig. 7).

inclusions and porosity. It should be stressed that the 2D representation was a compromise from the point of view of resolution and computational time. The use of 2D models as simplification of 3D microstructures for elastic calculations was validated in [14], in particular for composites with moderate contrasts between the elastic properties of the phases. This is expected to be the case at the cement paste scale, where the differences of elastic Young's moduli between the phases are within a factor of 3 or less (around 70 GPa for CH, fly ash and quartz and 22–28 GPa for C-S-H gel), except the clinker phase (elastic modulus of 130 GPa), whose concentration is however rather low (0.15). We assume that the validity of the 2D simulations should hold also for the viscoelastic behavior, especially when the viscoelastic phase (C-S-H matrix) is continuous also in the 2D model and the volume of the elastic inclusions is relatively low, as also argued in [51].

The similar stiffness of different phases should also lead to relatively low impact of morphology of phases on the model outcomes. A negligible effect of the shape of the stiff inclusions (circulars vs ellipsoidal aggregates) on the creep behavior was found with 2D modelling in [51] as long as the particles were oriented randomly; this is especially the case for cement paste (while random orientation is not necessarily found in mortars due to the effect of casting). Moreover, in the 3D modelling by Lavergne et al. [52] it was found that the creep behavior of a composite (mortar) was independent from the shape (spherical or angular) and size distributions of the stiff inclusions (aggregates) for size ratio of the inclusions 1/10. In 2D modelling [51], a negligible effect of size distribution of the stiff inclusions was observed, except when the largest inclusions were two orders of magnitude larger than the smallest. Such size difference should not be the case for the cement paste modelled here.

The largest effect of morphology is expected to happen at the lowest scale considered – that of the C-S-H gel and capillary porosity, mainly because the morphology is complex and not fully understood at this scale. Moreover, unlike at the higher scale of cement paste, where only solid phases are modelled, at the matrix scale there exists an extreme contrast in properties between the solid C-S-H gel and the porosity, which could lead to high differences between the 2D and 3D simulations [53]. For this reason, and also due to limitation of the resolution of the model, 3D microstructural modelling results from [14] were applied at this scale. Applying the scale factors from different microstructures (i.e. with different morphologies of porosity/solids) studied in [14] it was shown that although different absolute values of creep compliance of C-S-H gel were back-calculated, the general relation between porosity and macroscopic creep compliance was valid, i.e. an

intrinsic C-S-H gel compliance was found for systems with different porosities. We assume that the validity of this conclusion also holds for the cement paste scale represented by a 2D model.

To summarize, even though the 2D representation and the simplified geometry of the phases do not necessarily lead to the same quantitative results for the creep behavior (creep compliance) as would 3D modelling with more realistic morphology (as suggested by different creep compliances obtained with different microstructural modelling results from [14]), we expect that the validity of the result showing equal intrinsic creep of C-S-H between different systems should hold irrespective of using either simplified 2D or more complex 3D simulations.

5.2. Effect of fillers and SCMs on basic creep compliance

The unreacted fillers enhanced the creep magnitude, as shown in Fig. 4. The presence of quartz filler in a cementitious system has two opposite effects with regard to the viscous behavior. On the one hand, the quartz filler is a purely elastic material and induces an internal restraint in the cement paste. On the other hand, high quartz filler content increases the effective w/c (the w/c in CQZ35 was 0.63) and therefore the C-S-H together with water and pores would have higher creep compliance. This second effect seems to be prevailing in the experimental results presented here.

In the case of fly ash, it enhances the creep likely first due to increased w/c (the w/c is 0.58, similar effect as quartz fillers). For the effect of the pozzolanic reaction on creep, it is generally associated to its effect on strength and elastic Young's modulus [8,10]. Note that at 28 days, the elastic Young's modulus of CFA35 was lower than that of PC35, which also correlates with its higher creep. In terms of the microscale effect of the pozzolanic reaction, the reduction of porosity would reduce creep. The effect of an increase in the volume of C-S-H (due to the pozzolanic reaction) can be debated. Based on the solidification theory, an increase in the volume fraction of the C-S-H is accompanied by a decrease of porosity, therefore it should decrease creep [54]. On the contrary, based on the dissolution-precipitation theory [55], the process of dissolution of anhydrous phases and precipitation of hydration products would induce further creep.

5.3. Effect of fillers and SCMs on kinetics of creep compliance

According to Section 3.2.3, expressing the first derivative of the compliance in relation to $t - \tau$ highlights that the creep-rate of the studied blended cement pastes follows a power-law function (at least after 15 min from loading). The specific basic creep compliance of the cement paste CQZ35 was less precisely described by the power-law function. This single relationship has already been noticed for cement pastes [4] and for concrete [29].The relevance of this function for minute-long creep tests on hardening cement paste was also demonstrated in [21]. The exponents of the power-law identified by several authors are reported in Table 10 and are similar to the ones of the present work (see Table 4), with most values falling between 0.7 and 0.8.

Table 10
Power-law exponent reported in the literature.

References	Exponent
Tamtsia and Beaudoin [4]	$0.79 < \gamma < 0.86$
Rossi et al. [29]	$\gamma = 0.75$[*]
Torrenti and Le Roy [56]	$\gamma = -1$[**]
Irfan-ul Hassan et al. [21]	$0.7 < \gamma < 0.82$

[*] Value identified by the authors of this paper based on the result published by Rossi et al. [29].

[**] Value assumed by Torrenti and Le Roy [56] and in good agreement with experimental observations.

5.4. Viscoelastic behavior of C-S-H

The back-calculated viscoelastic behavior of the C-S-H based on the microstructural simulation suggests that a similar intrinsic behavior of the C-S-H gel can explain the creep kinetics of cement pastes with different blended binders. It seems that a change of the w/c does not affect the intrinsic creep behavior of the C-S-H considerably. Instead, the differences in macroscopic creep appear to be driven by changes of porosity above C-S-H matrix scale and by the presence of different SCM. However, based on the results of this study it is not possible to conclude how much the creep of the C-S-H gel will be affected by changes of w/c, since only three systems were compared for this parameter and the simulations of creep in 2D may not necessarily reflect the actual 3D behavior (see Section 5.1).

Regarding the effect of SCMs on the creep of C-S-H, the findings of this study are to be considered only preliminary, since only one system with fly ash of limited reactivity and one system with quartz filler were examined. Nevertheless, it is clear that the most important factor that needs to be considered in both numerical simulations and predictive models of creep is the porosity of the cement paste and the volume fractions of the different phases; these parameters are primarily related to the w/c (for the rather wide w/c range studied here, i.e. 0.35–0.63). Hence, as discussed in the previous paragraph, the intrinsic creep behavior of C-S-H appears to be independent from the presence of the SCM tested here and the differences in macroscopic creep behavior appear to be caused primarily by different w/c and corresponding porosity. It is however possible that, with changes of the chemical composition of the C-S-H and of the amount of gel porosity caused by some SCM, the viscoelastic behavior of the C-S-H gel would change.

The viscoelastic behavior of the C-S-H was studied by different researchers in the past, using nano-indentation [57] or with downscaling simulations by multiscale models [22]. In [57], a logarithmic evolution of the viscoelastic behavior of C-S-H was identified, while in both this study and in [22], a power law evolution was found. These differences may be due to the fact that longer term creep was considered in [57]. Moreover, higher creep of C-S-H was found in [22], which may due to different microstructures used in the models, especially at the C-S-H matrix scale (in [22], it was called C-S-H foam and C-S-H was considered as needle-shaped).

By assuming an intrinsic viscoelastic behavior of the C-S-H, Li et al. [58] simulated both the apparent and the intrinsic viscoelastic relaxation of hydrating cement paste with different w/c using a 3D FEM model equipped with the hydration modelling framework THAMES. It is worth noting that the viscoelastic behavior obtained with our 2D microstructural modelling agrees relatively well with that assumed for the simulations in [58].

In this study, the two-cut GRF model was selected among the seven statistical models [14] to calculate the viscoelastic behavior of the C-S-H. As previously mentioned, the reason for selecting this model was that it provided the best agreement of the estimated elastic modulus with the nano-indentation data, see Section 4.3. To shed light on the influence of the choice of the statistical model on the results, the solid spheres model, which provided the lowest values of the scale factor, was also used (see Fig. 7). The creep results of the C-S-H gel calculated with this second model are presented in Fig. 10. It appears that applying this extreme model still leads to the back-calculation of very similar (intrinsic) creep behavior of the C-S-H gel for the systems PC35, PC40 and CFA35. The creep magnitude is in this case lower compared to the two-cut GRF model, owing to the lower values of the scale factor. A clearly different creep was predicted for the system with quartz CQZ35. This is due to a very low solid fraction of this system (0.54) compared to the other systems tested here, see Table 9, leading to the extremely low value of the scale factor. It should be noted that this low solid fraction is at the limit of the applicability of the statistical model, see Fig. 7. These observations underline that the impact of the porosity's morphology on the viscoelastic behavior needs to be considered for a properly
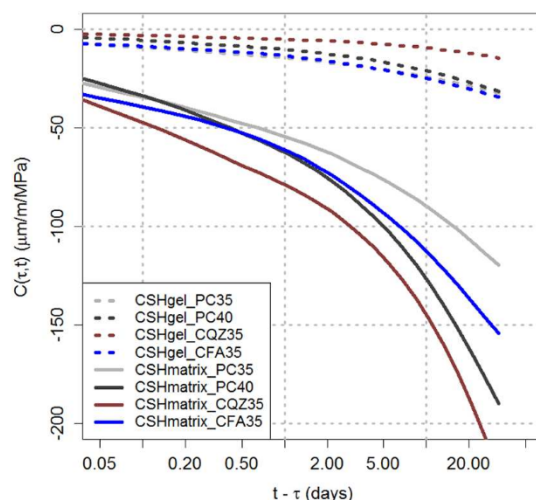

Fig. 10. Comparison of back-calculated viscoelastic behavior (specific basic creep compliance) of C-S-H matrix and C-S-H gel in four systems (scale factor based on the solid spheres model, see Fig. 7).

quantitative prediction. This is especially the case for highly porous systems (high w/c or at early age). Therefore, considering that this outlying curve corresponds to the extremely low solid fraction and that the other statistical models would yield closer creep behavior for all systems tested here, the conclusion of the similar creep behavior of the C-S-H gel (hence, intrinsic creep of the C-S-H gel) can be supported.

It should be noted that our work focused on creep in mature (older than 28 d) cement pastes. Considering the very low hydration rates occurring at such late age and the high overall hydration degree (0.7 in w/c 0.35 cement paste [59]), we assumed that the microstructure was not evolving during the time after loading and hence assumed negligible creep aging. This further allows us to assume that the back-calculated creep compliance is in major part due to intrinsic creep behavior of the C-S-H and not due to other mechanisms, e.g. hydration-related creep (dissolution-driven creep) see [58,60].

6. Conclusions

In this paper, a quantitative study and an evaluation of the experimentally studied basic creep behavior of cement pastes with different water-to-binder ratio and with and without fly ash or quartz filler were presented.

The creep response of the systems with fly ash or quartz filler was higher than of the corresponding pure cement paste of the same w/b. In order to shed light on the reasons of the higher creep compliance of the systems with quartz and fly ash, microstructural simulations were carried out. First, the viscoelastic properties of the C-S-H matrix (C-S-H gel + capillary pores) were back-calculated with FEM simulations based on the macroscopic creep measurements on cement pastes and the volumetric composition of the cement pastes. 2D simulations were carried out with circular inclusions of sizes characteristic for different phases. After obtaining the elastic Young's modulus and the creep compliance of the C-S-H matrix with this approach, the intrinsic properties of the C-S-H gel could be calculated by an additional back-calculation step (from porous matrix to C-S-H gel) with 3D microstructural modelling results from [14]. This step was based on the assumption that the ratio between the strains of the solid (C-S-H gel) and of the porous body (C-S-H matrix), so-called scale factor, is the same for both elastic and viscoelastic strains. The statistical model with its underlying morphology for calculating the scale factor was selected based on the best agreement of the back-calculated elastic Young's modulus of the C-S-H gel with the experimental data in the literature. Additionally, another statistical model with considerably different underlying

morphology was also applied to assess the effect on the model outcomes.

Using these approaches, it was found that the apparent differences in the creep compliance between the different systems prepared with different w/c and blended with fly ash or quartz (resulting in w/c in the range 0.35–0.63) can be, in major part, explained by their different capillary porosities (which are primarily related to their different w/c), whereas the intrinsic creep compliance of the C-S-H gel appeared to be similar. When the assumptions regarding the underlying morphology and the microstructural modelling result from [14] for down-scaling of the C-S-H gel properties are altered, the calculated intrinsic compliance of the C-S-H gel changes, however the conclusion of similar intrinsic C-S-H creep in different systems still holds.

Acknowledgements

References

[1] Z.R. Bažant, G.H. Li, Comprehensive database on concrete creep and shrinkage, ACI Mater. J. 105 (2008) 635–637.

[2] M.A. Ward, A.M. Neville, S.P. Singh, Creep of air-entrained concrete, Mag. Concr. Res. 21 (1969) 205–210.

[3] R. Le Roy, Déformations instantanées et différées des béton a hautes performances, Ecole Nationale des Ponts et Chaussees, 1995.

[4] B.T. Tamtsia, J.J. Beaudoin, Basic creep of hardened cement paste. A re-examination of the role of water, Cem. Concr. Res. 30 (2000) 1465–1475.

[5] A.M. Neville, Creep of concrete as a function of its cement paste content, Mag. Concr. Res. 16 (1964) 21–30.

[6] L. Granger, Comportement différé du béton dans les enceintes de centrales nucléaires: analyse et modélisation, Ecole Nationale des Ponts et Chaussees, 1995.

[7] G.M. Ji, T. Kanstad, Ø. Bjøntegaard, E.J. Sellevold, Tensile and compressive creep deformations of hardening concrete containing mineral additives, Mater. Struct. 46 (2013) 1167–1182.

[8] I. Pane, W. Hansen, W. Hansen, Early age creep and stress relaxation of concrete containing blended cements, Mater. Struct. 35 (2002) 92–96.

[9] A.E. Klausen, T. Kanstad, E. Sellevold, Comparison of tensile and compressive creep of fly ash concretes in the hardening phase, Cem. Concr. Res. 95 (2017) 188–194.

[10] M. Shariq, J. Prasad, H. Abbas, Creep and drying shrinkage of concrete containing GGBFS, Cem. Concr. Compos. 68 (2016) 35–45.

[11] M. Vandamme, F.J. Ulm, Nanoindentation investigation of creep properties of calcium silicate hydrates, Cem. Concr. Res. 52 (2013) 38–52.

[12] D.T. Nguyen, R. Alizadeh, J.J. Beaudoin, P. Pourbeik, L. Raki, Microindentation creep of monophasic calcium-silicate-hydrates, Cem. Concr. Compos. 48 (2014) 118–126.

[13] C.F. Dunant, K.L. Scrivener, Micro-mechanical modelling of alkali–silica-reaction-induced degradation using the AMIE framework, Cem. Concr. Res. 40 (2010) 517–525.

[14] A.P. Roberts, E.J. Garboczi, Computation of the linear elastic properties of random porous materials with a wide variety of microstructure, R. Soc. 458 (2002) 1033–1054.

[15] P.T. Durdziński, M. Ben Haha, S.A. Bernal, N. De Belie, G. Elke, B. Lothenbach, J.L. Provis, A. Schöler, C. Stabler, Z. Tan, A. Vollpracht, F. Winnefeld, Y. Villagrán Zaccardi, M. Zajac, K.L. Scrivener, Outcomes of the RILEM round robin on degree of reaction of slag and fly ash in blended cements, Mater. Struct. 50 (2017) 135.

[16] S. 505 262/1, Construction en béton – Spécifications complémentaires, (2003), pp. 1–28.

[17] ASTM, ASTM C1698-09:Standard Test Method for Autogenous Strain of Cement Paste and Mortar, (2009).

[18] O. Mejlhede Jensen, P. Freiesleben Hansen, A dilatometer for measuring autogenous deformation in hardening Portland cement paste, Mater. Struct. 28 (1995) 406–410.

[19] M. Wyrzykowski, Z. Hu, S. Ghourchian, K. Scrivener, P. Lura, Corrugated tube protocol for autogenous shrinkage measurements: review and statistical assessment, Mater. Struct. (2017) 50–57.

[20] ASTM, ASTM C512 - standard test method for creep of concrete in compression, Am. Soc. Test. Mater. (2010) 1–5.

[21] M. Irfan-Ul-Hassan, B. Pichler, R. Reihsner, C. Hellmich, Elastic and creep properties of young cement paste, as determined from hourly repeated minute-long quasi-static tests, Cem. Concr. Res. 82 (2016) 36–49.

[22] M. Königsberger, M. Irfan-ul-Hassan, B. Pichler, C. Hellmich, Downscaling based identification of nonaging power-law creep of cement hydrates, J. Eng. Mech. 142 (2016) 04016106.

[23] W. Hansen, Drying shrinkage mechanisms in Portland cement paste, J. Am. Ceram. Soc. 70 (1987) 323–328.

[24] J.J. Brooks, 30-year creep and shrinkage of concrete, Mag. Concr. Res. 57 (2005) 545–556.

[25] A.-M. Poppe, G. De Schutter, Creep and shrinkage of self-compacting concrete, SCC'2005-China 1st Int. Symp. Des. Perform. Use Self-Consolidating Concr, 2005, pp. 329–336.

[26] J.M. Torrenti, R. Leroy, J.M. Torrenti, R. Leroy, J.M. Torrenti, R. Leroy, Analyse et modélisation du fluage propre du béton (To cite this version: Analyse et modélisation du fluage propre du béton), (2015).

[27] A.S. Lubansky, Y.L. Yeow, Y.-K. Leong, S.R. Wickramasinghe, B. Han, A general method of computing the derivative of experimental data, AICHE J. 52 (2006) 323–332.

[28] R. Kohavi, A study of cross-validation and bootstrap for accuracy estimation and model selection, Int. Jt. Conf. Artif. Intell, 1995.

[29] P. Rossi, J.L. Tailhan, F. Le Maou, Creep strain versus residual strain of a concrete loaded under various levels of compressive stress, Cem. Concr. Res. 51 (2013) 32–37.

[30] RILEM, Creep and shrinkage prediction model for analysis and design of concrete structures-model B3, Mater. Struct. 3 (1995) 357–365.

[31] F. Lavergne, K. Sab, J. Sanahuja, M. Bornert, C. Toulemonde, An approximate multiscale model for aging viscoelastic materials exhibiting time-dependent Poisson's ratio, Cem. Concr. Res. 86 (2016) 42–54.

[32] Q. Do, Modelling Properties of Cement Paste From Microstructure : Porosity, Mechanical Properties, Creep and Shrinkage, EPFL, 2013.

[33] P.T. Durdziński, M. Ben Haha, M. Zajac, K.L. Scrivener, Phase assemblage of composite cements, Cem. Concr. Res. 99 (2017) 172–182.

[34] A.C.A. Muller, K.L. Scrivener, A.M. Gajewicz, P.J. McDonald, Use of bench-top NMR to measure the density, composition and desorption isotherm of C-S-H in cement paste, Microporous Mesoporous Mater. 178 (2013) 99–103.

[35] N. Schwarz, N. Neithalath, Influence of a fine glass powder on cement hydration: comparison to fly ash and modeling the degree of hydration, Cem. Concr. Res. 38 (2008) 429–436.

[36] P.T. Durdziński, C.F. Dunant, M. Ben Haha, K.L. Scrivener, A new quantification method based on SEM-EDS to assess fly ash composition and study the reaction of its individual components in hydrating cement paste, Cem. Concr. Res. 73 (2015) 111–122.

[37] M. Hlobil, V. Smilauer, G. Chanvillard, Multiscale micromechanical damage model for compressive strength based on cement paste microstructure, CONCREEP, 10 2015, pp. 1211–1218.

[38] A.B. Giorla, K.L. Scrivener, C.F. Dunant, Finite elements in space and time for the analysis of generalised visco-elastic materials, Int. J. Numer. Methods Eng. 97 (2014) 454–472.

[39] K. Velez, S. Maximilien, D. Damidot, G. Fantozzi, F. Sorrentino, Determination by nanoindentation of elastic modulus and hardness of pure constituents of Portland cement clinker, Cem. Concr. Res. 31 (2001) 555–561.

[40] G. Constantinides, F.-J. Ulm, The effect of two types of C-S-H on the elasticity of cement-based materials: results from nanoindentation and micromechanical modeling, Cem. Concr. Res. 34 (2004) 67–80.

[41] Quartz|Quartz Grinding|Ceramic Quartz|Quartz Properties, (n.d.). http://www.ferroceramic.com/quart_table.htm.

[42] F. Deschner, B. Lothenbach, F. Winnefeld, J. Neubauer, Effect of temperature on the hydration of Portland cement blended with siliceous fly ash, Cem. Concr. Res. 52 (2013) 169–181.

[43] E.M. Foley, J.J. Kim, M.M. Reda Taha, Synthesis and nano-mechanical characterization of calcium-silicate-hydrate (C-S-H) made with 1.5 CaO/SiO2 mixture, Cem. Concr. Res. 42 (2012) 1225–1232.

[44] G. Geng, R.J. Myers, J. Li, R. Maboudian, C. Carraro, D.A. Shapiro, P.J.M. Monteiro, Aluminum-induced dreierketten chain cross-links increase the mechanical properties of nanocrystalline calcium aluminosilicate hydrate, Sci. Rep. 7 (2017) 1–10.

[45] J.E. Oh, S.M. Clark, P.J.M. Monteiro, Does the Al substitution in C-S-H(I) change its mechanical property? Cem. Concr. Res. 41 (2011) 102–106.

[46] P.J. McDonald, V. Rodin, A. Valori, Characterisation of intra- and inter–C–S–H gel pore water in white cement based on an analysis of NMR signal amplitudes as a function of water content, Cem. Concr. Res. 40 (2010) 1656–1663.

[47] R.M. Spriggs, T. Vasilos, Functional relation between creep rate and porosity for polycrystalline ceramics, J. Am. Ceram. Soc. 47 (1964) 47–48.

[48] C. Pichler, R. Lackner, H.A. Mang, Multiscale model for creep of shotcrete -from logarithmic-type viscous behavior of CSH at the µm-scale to macroscopic tunnel analysis, J. Adv. Concr. Technol. 6 (2008) 91–110.

[49] Y. Wei, D. Ph, S. Liang, X. Gao, Simulation of porosity effect on mechanical and creep properties of cement paste at microscale, Sixth Biot Conf. Poromechanics, 2017, pp. 1099–1107.

[50] Q.V. Le, F. Meftah, Q.C. He, Y. Le Pape, Creep and relaxation functions of a heterogeneous viscoelastic porous medium using the Mori-Tanaka homogenization scheme and a discrete microscopic retardation spectrum, Mech. Time-Depend. Mater. 11 (2007) 309–331.

[51] A.B. Giorla, C.F. Dunant, Microstructural effects in the simulation of creep of concrete, Cem. Concr. Res. 105 (2018) 44–53.

[52] F. Lavergne, K. Sab, J. Sanahuja, M. Bornert, C. Toulemonde, Investigation of the effect of aggregates' morphology on concrete creep properties by numerical simulations, Cem. Concr. Res. 71 (2015) 14–28.

[53] S. Meille, E.J. Garboczi, Linear elastic properties of 2D and 3D models of porous materials made from elongated objects, Model. Simul. Mater. Sci. Eng. 9 (2001) 371–390.

[54] Z.P. Bažant, P. Santosh, Solidification theory for concrete creep, J. Eng. Mech. 115 (1989) 1691–1703.

[55] E.A. Pachon-Rodriguez, E. Guillon, G. Houvenaghel, J. Colombani, Wet creep of hardened hydraulic cements - example of gypsum plaster and implication for hydrated Portland cement, Cem. Concr. Res. 63 (2014) 67–74.

[56] J.M. Torrenti, R. Le Roy, Analysis and modelling of basic creep, CONCREEP 10, 2015, pp. 1400–1409.

[57] M. Vandamme, F.-J. Ulm, Nanogranular origin of concrete creep, Proc. Natl. Acad. Sci. U. S. A. 106 (2009) 10552–10557.

[58] X. Li, Z.C. Grasley, E.J. Garboczi, J.W. Bullard, Modeling the apparent and intrinsic viscoelastic relaxation of hydrating cement paste, Cem. Concr. Compos. 55 (2015) 322–330.

[59] Z. Hu, Prediction of Autogenous Shrinkage in Fly Ash Blended Cement Systems, EPFL, 2017.

[60] M. Wyrzykowski, K. Scrivener, P. Lura, Basic creep of cement paste at early age - the role of cement hydration, Cem. Concr. Res. 116 (2019) 191–201.